

HST/WFC3 transmission spectroscopy of the cold rocky planet TRAPPIST-1h

L. J. Garcia¹, S. E. Moran^{2,3}, B. V. Rackham^{4,5} *, H. R. Wakeford⁶, M. Gillon¹, J. de Wit⁷, and N. K. Lewis⁸

¹ Astrobiology Research Unit, Université de Liège, Allée du 6 Août 19C, B-4000 Liège, Belgium
e-mail: lgarcia@uliege.be

² Department of Earth and Planetary Sciences, Johns Hopkins University, 3400 N Charles St, Baltimore, MD 21218, USA

³ Bay Area Environmental Research Institute/NASA Ames Research Center, Moffett Field, CA 94035, USA

⁴ Department of Earth, Atmospheric and Planetary Sciences, Massachusetts Institute of Technology, 77 Massachusetts Avenue, Cambridge, MA 02139, USA

⁵ Kavli Institute for Astrophysics and Space Research, Massachusetts Institute of Technology, Cambridge, MA 02139, USA

⁶ School of Physics, University of Bristol, HH Wills Physics Laboratory, Tyndall Avenue, Bristol BS8 1TL, UK

⁷ Department of Earth, Atmospheric and Planetary Sciences, Massachusetts Institute of Technology, 77 Massachusetts Avenue, Cambridge, MA 02139, USA

⁸ Department of Astronomy and Carl Sagan Institute, Cornell University, 122 Sciences Drive, Ithaca, NY 14853, USA

ABSTRACT

Context. TRAPPIST-1 is a nearby ultra-cool dwarf star transited by seven rocky planets. We observed three transits of its outermost planet, TRAPPIST-1h, using the G141 grism of the Wide Field Camera 3 instrument aboard the Hubble Space Telescope to place constraints on its potentially cold atmosphere

Aims. In order to deal with the effect of stellar contamination, we model TRAPPIST-1 active regions as portions of a cooler and a hotter photosphere, and generate multi-temperature models that we compare to the out-of-transit spectrum of the star. Using the inferred spot parameters, we produce corrected transmission spectra for planet h under five transit configurations and compare these data to planetary atmospheric transmission models using the forward model CHIMERA.

Methods. Our analysis reveals that TRAPPIST-1h is unlikely to host an aerosol-free H/He-dominated atmosphere. While the current data precision limits the constraints we can put on the planetary atmosphere, we find that the likeliest scenario is that of a flat, featureless transmission spectrum in the WFC3/G141 bandpass due to a high mean molecular weight atmosphere ($\geq 1000\times$ solar), no atmosphere, or an opaque aerosol layer, all in absence of stellar contamination. This work outlines the limitations of modeling active photospheric regions with theoretical stellar spectra, and those brought by our lack of knowledge of the photospheric structure of ultracool dwarf stars. Further characterization of the planetary atmosphere of TRAPPIST-1h would require higher precision measurements over wider wavelengths, which will be possible with the James Webb Space Telescope (JWST).

Results.

Conclusions.

Key words. planets and satellites: atmospheres – infrared: planetary systems – stars: low-mass – (stars:) starspots - methods: data analysis

1. Introduction

While the first detailed atmospheric characterizations of giant exoplanets were carried out during the last two decades (e.g., Charbonneau et al. 2002; Deming et al. 2013), the study of smaller planets, that is those comparable to the size of Earth, will become increasingly accessible in the near future. This is especially true for planets orbiting nearby M-dwarfs, offering larger transit signal-to-noise ratios compared to small planets transiting larger stars (Charbonneau 2009). This makes the seven planets orbiting TRAPPIST-1, an M8-type dwarf star located 12 parsec away (Gillon et al. 2017; Luger et al. 2017), excellent candidates for detailed atmospheric characterizations with the upcoming James Webb Space Telescope (Morley et al. 2017; Lustig-Yaeger et al. 2019). So far, spectroscopic observations from the Hubble Space Telescope Wide Field Camera 3 (HST/WFC3) have been able to rule out the presence of clear primary hydrogen-dominated atmospheres for all

planets (de Wit et al. 2016, 2018; Wakeford et al. 2019) except for the outermost planet, TRAPPIST-1h, the most likely to have retained such an extended atmosphere (Bourrier et al. 2017).

The technique of transit spectroscopy, which consists in measuring a planet's transit depths at different wavelengths, remains one of the most successful methods to partially characterize exoplanets atmospheres. However, this method brings with it a major challenge: the effect of stellar contamination (e.g., Pont et al. 2008; Apai et al. 2018). Indeed, any spectral difference between the transited chord and the rest of the stellar disk can result in signals of stellar origin able to mimic or hide those of planetary ones (Rackham et al. 2018, 2019b). This concern has led the exoplanetary science community to explore a number of solutions (e.g., Rackham et al. 2019a), some based on the modeling of active regions probed by the planet during its transit (e.g., Espinoza et al. 2019), and others addressing the contamination from unocculted active regions (e.g., Wakeford

* 51 Pegasi b Fellow

et al. 2019).

In this work, we present the transmission spectrum of TRAPPIST-1h obtained from HST/WFC3 observations in order to rule out the presence of an extended hydrogen-rich atmosphere. We describe our three transit observations and their time-resolved spectra extraction in section 2. In section 3, we model the spectroscopic light curves obtained from these measurements, leading to a joint transmission spectrum. We then attempt to model the out-of-transit spectra of TRAPPIST-1 in section 4 in order to deal with the effect of stellar contamination by following the approach of Rackham et al. (2018) and Wakeford et al. (2019). By assuming five possible transit configurations, we model the planetary component of the measured spectrum in section 5. Finally, we discuss the results of these models and give our conclusions in section 6.

2. Observations

We observed three transits of TRAPPIST-1h with the Hubble Space Telescope (HST) Wide Field Camera 3 (WFC3) as part of HST GO program 15304 (PI: J. de Wit) on UT 2018 July 19 (visit 1), 2019 September 24 (visit 2), and 2020 July 20 (visit 3)¹. Each of the three transits was observed over a five-hour window, each requiring four HST orbits, all consisting in approximately 45 minutes of observation separated by 45 minute gaps due to Earth occultation. We obtained time-series spectroscopy in the 1.12–1.65 μm wavelength band using the G141 grism in scanning mode, spreading the stellar spectrum perpendicularly to its dispersion axis. The scan rate was set to 0'02 s⁻¹ with an exposure time of 112 s, resulting in 17-pixel-wide scans acquired in the forward direction only. Each scan is composed of six non-destructive readouts (including the zeroth-read), which we used in our reduction process to remove part of the accumulated background over the complete exposures. A direct image of the target was acquired using the F139M narrow-band filter at the beginning of each orbit in order to perform G141 wavelength calibration.

Data reduction

We extracted the time-resolved spectra from the three visits following the method presented by Kreidberg et al. (2014) and using the *prose*² Python framework (Garcia et al. 2021). *prose* is a general-purpose tool to build modular astronomical pipelines out of reusable and well-maintained processing blocks. As in Kreidberg et al. (2014), we start from the *ima* pre-calibrated products and process each image through the same steps. As described in section 2, the full spectrum in an image is spread along the spatial direction of the detector. During the process, nondestructive readouts are recorded such that a specific subexposure can be constructed by subtracting its readout from the previous one, hence removing part of the accumulated background. We then start by forming subexposures out of nondestructive readouts. For each subexposure:

1. we mask bad pixels identified from the *calcfwfc3* pipeline
2. we compute the wavelength trace using a direct image of the source and the solution from Pirzkal et al. (2016)

3. we apply a wavelength-dependent flat-field calibration using the method of Kuntschner et al. (2011)
4. we interpolate all image rows to the wavelength solution of the direct image so that all values found in a given column correspond to photons from a common wavelength bin
5. we estimate the subexposure background as the median pixel value within a spectrum-free portion of the image, which we subtract from the subexposure
6. we cut the spectrum out of the image using a 40-pixel-tall aperture centered in the scanning direction on the spectrum center of light. This large aperture (compared to the 17-pixel-tall spectrum) is manually set in order to include the tail of the WFC3/IR point spread function
7. we extract a 1D spectrum from this cutout using an optimal-spectrum-extraction algorithm (Horne 1986). By using this technique, the fact that more background pixels are contained in our wide aperture does not affect the noise of our extracted signal, as these are optimally weighted.

Once these seven steps are completed for all subexposures of an image, we interpolate the subexposure spectra to a common wavelength axis and sum them, which yields the final 1D spectrum of the image. Each of the steps described above, applied to an image and its subexposures, are implemented into modular *prose* blocks, and then assembled into a reduction pipeline made available to the community through the *prose* Python package.

In parallel, we performed a comparative extraction of the spectra from the three visits using *iraclis*³, an open-source Python package presented by Tsiaras et al. (2016). Its reduction starts from the raw observation products and goes through the calibration steps of the *calcfwfc3* pipeline⁴. Then, for every image, the wavelength-dependent photon trajectories along the scanned spectrum are computed, so that fluxes can be extracted within accurately placed polygonal boxes along the wavelength trace (see Tsiaras et al. 2016, Figure 6). By doing so, the method used in *iraclis* properly accounts for the off-axis nature of the G141 slitless spectra and refines the wavelength solution of every exposure.

The spectra obtained from *iraclis* are directly extracted within wavelength bins that we also apply to the *prose* spectra: 12 bins from 1.1 μm to 1.67 μm , leading to bins of $\sim 0.04 \mu\text{m}$ in width. This sampling is chosen to form wavelength bins including complete pixels in the dispersion axis.

The raw data obtained this way feature ramp-like signals characteristic of WFC3 observations. In order to consistently model these signals over all orbits, we discard the first orbit of each visit, which features a higher-amplitude ramp. For the same reason, we discard the first and second exposures of each orbit. The white-light curves from the three visits are shown in Figure 1 (raw data are in light gray) and were obtained by summing the spectra over all wavelength bins.

¹ These three visits are respectively denoted 03, 02 and 04 in the observing plan

² <https://github.com/lgrcia/prose>

³ <https://github.com/ucl-exoplanets/Iraclis>

⁴ <https://hst-docs.stsci.edu/wfc3dhh/chapter-3-wfc3-data-calibration/3-3-ir-data-calibration-steps>

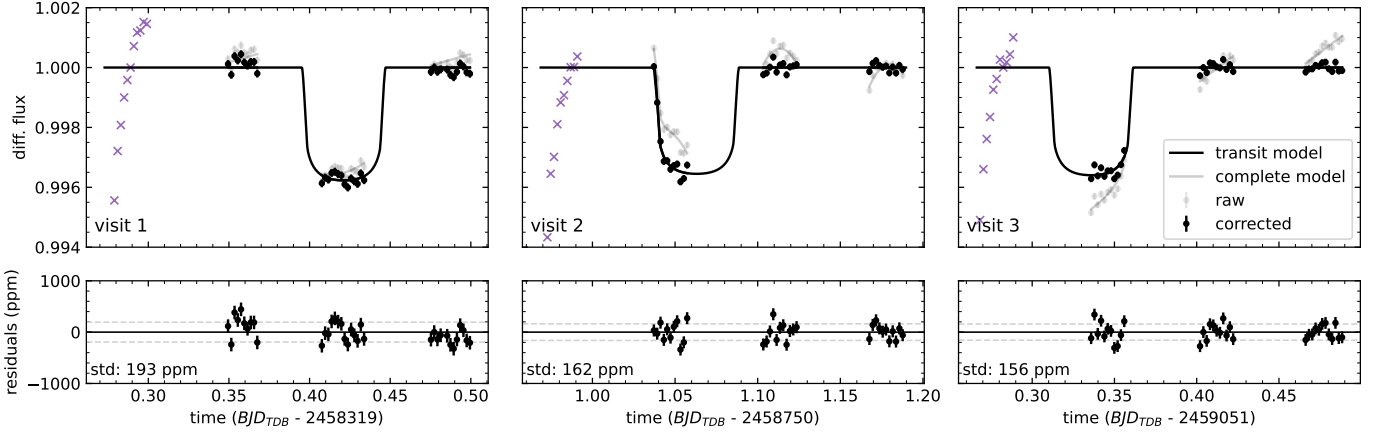


Fig. 1. White-light curves of visit 1, 2, and 3 of GO 15304 observations. The first orbit is plotted as purple crosses and is not used in the analysis.

parameter	unit	value
R_\star	R_\odot	$\mathcal{N}(0.1192, 0.0013)$
M_\star	M_\odot	$\mathcal{N}(0.0898, 0.0023)$
P	days	$\mathcal{N}(18.7672745, 0.00001876)$
b	-	$\mathcal{N}(0.448, 0.054)$
T_0	BJD tdb	$\mathcal{U}(t_0, t_f)$

Table 1. Priors on TRAPPIST-1 stellar parameters and TRAPPIST-1h orbital parameters. R_\star and M_\star are respectively the stellar radius and mass with prior distributions from Agol et al. (2021). P and b are TRAPPIST-1h orbital period and impact parameters taken from Ducrot et al. (2020). T_0 is the transit mid-time, and the transit depth is set to an uninformative uniform prior. $\mathcal{U}(a, b)$ denotes a uniform distribution bounded by (a, b) , and $\mathcal{N}(\mu, \sigma)$ a normal distribution of variance σ^2 centered on μ . t_0 and t_f correspond to the times of the first and last exposures of a given visit.

Bandpass (μm)	u_1	u_2
1.101 - 1.119	0.167 ± 0.020	0.373 ± 0.029
1.140 - 1.159	0.168 ± 0.020	0.384 ± 0.030
1.180 - 1.200	0.175 ± 0.020	0.385 ± 0.029
1.222 - 1.242	0.150 ± 0.019	0.362 ± 0.028
1.265 - 1.286	0.146 ± 0.018	0.338 ± 0.026
1.310 - 1.332	0.177 ± 0.018	0.352 ± 0.026
1.355 - 1.379	0.230 ± 0.019	0.410 ± 0.028
1.403 - 1.428	0.326 ± 0.014	0.359 ± 0.021
1.453 - 1.479	0.289 ± 0.016	0.378 ± 0.023
1.504 - 1.530	0.224 ± 0.019	0.396 ± 0.027
1.558 - 1.585	0.178 ± 0.019	0.373 ± 0.027
1.612 - 1.641	0.135 ± 0.018	0.331 ± 0.026

Table 2. Quadratic limb darkening parameters obtained from ExoCTK (Bourque et al. 2021).

3. Light-curve modeling

In the following sections, we present our modeling of the transmission spectra obtained from *iracis* and *prose* and validate our results based on their comparison.

3.1. Systematic models comparison

Spectroscopic light curves obtained with HST display a high level of wavelength-, visit-, and orbit-dependent systematic signals (Wakeford et al. 2016 and references therein). Similarly to

previous studies, we model these signals using empirical functions of time t and HST orbital phase ϕ , which can take a variety of forms. For this study, we employ polynomials such that the white-light curve of a given visit can be modeled as:

$$F(t, \phi) = T(t) + P(t, \phi) + \epsilon(t), \quad (1)$$

where T is the transit light curve model, P is a polynomial systematic model of time t and HST orbital phase ϕ , and ϵ is a Gaussian noise vector. As in Wakeford et al. (2016), we selected the combination of polynomial orders of t and ϕ through a model comparison based on the minimization of the Akaike information criterion (AIC, Akaike 1974), such that our models are predictive while being limited in the number of parameters included. By allowing polynomials of up to order three and excluding cross terms, we end up with a set of 16 models to compare.

For a given visit and for each order combination, we infer the best transit and systematic model parameters in a Bayesian framework using *exoplanet* (Foreman-Mackey et al. 2021)⁵, making use of the inference framework *PyMC3*⁶ (Salvatier et al. 2016a) and the transit light curve model from Luger et al. (2019). The priors we use for the orbital parameters of TRAPPIST-1h are listed in Table 1, with T_0 having a uniform prior over the full time of the visit. This uninformative prior on the mid-transit time is used to encompass the wide transit time variations (TTVs) observed for the TRAPPIST-1 planets, reaching more than 1 hour for TRAPPIST-1h (Agol et al. 2021, Figure 2). Finally, we use a quadratic limb-darkening model with parameters fixed to the values in Table 2, obtained from ExoCTK⁷ (Bourque et al. 2021) using the PHOENIX ACES stellar atmosphere model (Husser et al. 2013).

Given our data, we find the maximum a posteriori model parameters using the BFGS algorithm (Head & Zerner 1985), as implemented in *scipy*⁸, and use this maximized posterior to compute the AIC for each order combination. Finally, for each visit, we retain the model with the minimal AIC (Figure A.1). While the best model is found by modeling the white-light curve of each visit, we also use it to model the systematic errors for the spectroscopic light curves, keeping the same form but allowing its parameters to vary from one wavelength bin to another.

⁵ <https://docs.exoplanet.codes/en/latest/>

⁶ <https://docs.pymc.io/>

⁷ https://exoctk.stsci.edu/limb_darkening

⁸ <https://docs.scipy.org/doc/scipy/reference/optimize.minimize-bfgs.html>

visit	transit time	systematics model
1	2458319.4206 ± 0.0030	$1 + \phi$
2	2458751.0660 ± 0.0003	$1 + \theta + \phi^2$
3	2459051.3365 ± 0.0008	$1 + \theta + \phi$

Table 3. Transit times inferred individually from each visit as well as the selected systematic error model

3.2. Transmission spectra inference

We model the spectroscopic light curves from each visit using the systematic models found in subsection 3.1, now using the wavelength-dependent expression of the flux:

$$F_{\lambda}(t, \phi) = T_{\lambda}(t) + P_{\lambda}(t, \phi) + \epsilon_{\lambda}(t), \quad (2)$$

and following the same notation as in Equation 1 with λ denoting the wavelength bin. As we are interested in the wavelength-dependent transit depth of TRAPPIST-1h, we set an uninformative prior on its wavelength-dependent radius:

$$R_{p,\lambda} \sim \mathcal{U}(0.5, 2)R_{\oplus}, \quad (3)$$

where $\mathcal{U}(a, b)$ is a uniform distribution bounded by a and b . Again, we use the orbital parameters and priors listed in Table 1. As in subsection 3.1, we adopt a quadratic limb-darkening model, the coefficients of which are held fixed to the values found in Table 2. For each visit, we estimate the wavelength-dependent transit depths and their uncertainties through an Hamiltonian Monte Carlo analysis of the data, making use of the *exoplanet* package (Foreman-Mackey et al. 2021).

Once this is done on individual visits (see the transmission spectra in Figure 3, left plot), we proceed to a global analysis of all visits using the priors listed in Table 1, and derive the global transmission spectrum shown in the right plot of Figure 3 with the spectroscopic light curves shown in Figure 2. We do that by allowing each visit to have its own systematic model, held to the ones found in the previous section (shown in Table 3) with free parameters. We verify that allowing for nonperiodic transits while accounting for transit time variations leads to the same transmission spectrum. Hence, we use the results obtained in the case of strictly periodic transits in the reminder of our analysis. The transit times obtained by considering each visit individually are reported in Table 3.

Finally, we check that the fluxes obtained from *prose* and *iracis* lead to similar transmission spectra. We also compare these transmission spectra to spectra obtained from an independent extraction, masking, and modeling following the methodology presented in Wakeford et al. (2019). The inferred transmission spectra are consistent across the three analyses (Figure A.2). Figure 3 highlights variations of the transmission spectra from one visit to another, which seem more pronounced at shorter wavelengths. To study the possible astrophysical origin of these variations, we proceed to the assessment of stellar contamination.

4. Stellar contamination

4.1. Photosphere model

To properly interpret the global transmission spectrum inferred in section 3, and to understand its variations between visits, we need to carefully assess the possible impact of stellar contamination on our transit observations. We adopt the same approach as Wakeford et al. (2019) by modeling the median out-of-transit spectrum of TRAPPIST-1, accounting for surface heterogeneities such as spots and faculae. Having a model of the

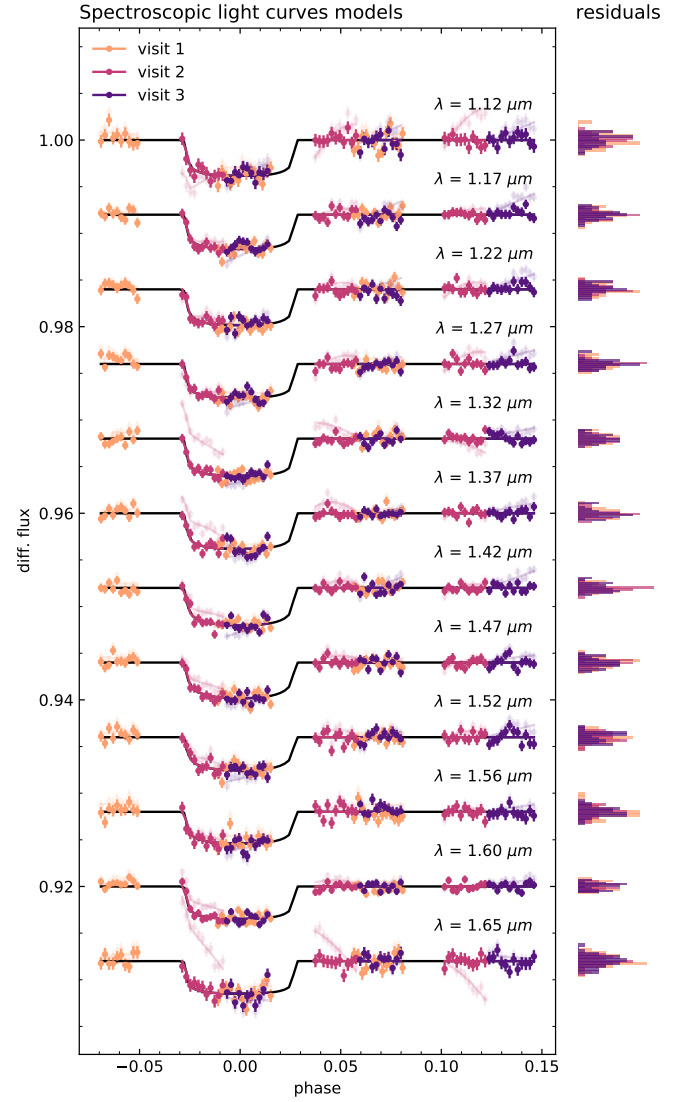


Fig. 2. Joint spectroscopic light-curve model for the three visits, each plotted with a single color. The raw data are represented by transparent points in the background, and systematic models overlaid as transparent lines. Solid points correspond to light curves corrected for the systematic error models, and solid black lines correspond to the inferred transit models per wavelength band. Finally, histograms of the residuals between the data and models are plotted to the right of each spectroscopic light curve.

stellar disk alone then allows us to correct the measured transmission spectrum from the stellar one, given the portion of the photosphere that is occulted. As in previous studies (e.g., Rackham et al. 2018, 2019b), we assume that the complete photosphere can be modeled as a combination of portions of cooler and hotter areas so that the spectrum of the star can be expressed as:

$$F = (1 - s - f)F_{phot} + sF_{spot} + fF_{fac}, \quad (4)$$

where s and f are the covering fractions of spots and faculae (here simply denoting the cooler and hotter portions of the photosphere) and F_{phot} , F_{spot} , and F_{fac} are the intrinsic spectra of the quiescent photosphere, spots, and faculae, respectively. This simple model assumes that surface heterogeneities have spectra

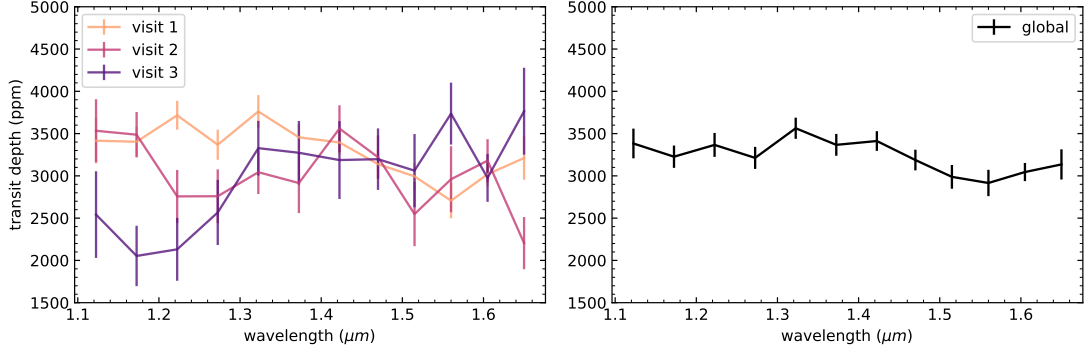


Fig. 3. Transmission spectra obtained for each visit individually (left) as well as the one obtained through a joint analysis (right).

similar to that of a global photosphere of a different temperature. We note that covering fractions f and s can be null, meaning that the model reduces to only one or two temperature components. To model the individual components of the TRAPPIST-1 photosphere, we use the BT-Settl stellar atmosphere models (Allard et al. 2012), which are specifically suited for cool stars, down to 1500K. Given that our observations are conducted in the infrared, these are more sensitive to cooler components, which justifies the choice of a model available at cooler temperatures.

4.2. Models and data preparation

Fitting Equation 4 to our data requires some preliminary steps. Indeed, BT-Settl theoretical spectra are provided on a grid of stellar metallicities, log-gravity, and effective temperatures. From this grid, we only keep spectra corresponding to $[Fe/H] = 0$, which is close to the inferred value of $[Fe/H] = 0.04$ (Van Grootel et al. 2018). We linearly interpolate the models along the log-gravity parameter in order to produce spectra with $\log_{10}(g) = 5.22$ (Van Grootel et al. 2018). By fixing these values, only the effective temperature of the models will be varied during their inference (except for the case discussed in subsection 4.3), ranging from 1500K to 5000K in steps of 100K. We then convert these models to flux density at Earth, accounting for TRAPPIST-1’s angular diameter, which is calculated as, $\alpha = (R_{\star}/d)^2$ using the stellar radius $R_{\star} = 0.119 R_{\odot}$ (Agol et al. 2021) and the distance $d = 40.54$ ly (Gaia Collaboration et al. 2018, DR2). Finally, we convolve the models with the WFC3 point spread function⁹ and sample them according to the WFC3 IR detector (50Å pixels).

The dataset we model consists of three out-of-transit spectra of TRAPPIST-1, one for each visit, and we fit each of them to a theoretical model. For each visit, we build a median spectrum over time, from which we correct the systematic signal that strongly affects the variations of its mean value (as modeled in subsection 3.1 and shown in Figure 2). To be compared with the models, we convert these spectra from $e^{-} s^{-1} \text{Å}^{-1}$ to $\text{erg s}^{-1} \text{cm}^{-2} \text{Å}^{-1}$ by correcting for the WFC3 IR detector sensitivity¹⁰, accounting for exposure time (112 s) and wavelength passband. WFC3 sensitivity quickly drops to zero outside of the band it covers, meaning that correcting for it (through division) leads to large errors on the tails of our spectra. While we could account for it in the fitting procedure,

we find a better convergence by trimming the measured spectra to the 1.15–1.63 μm band (see Figure 4).

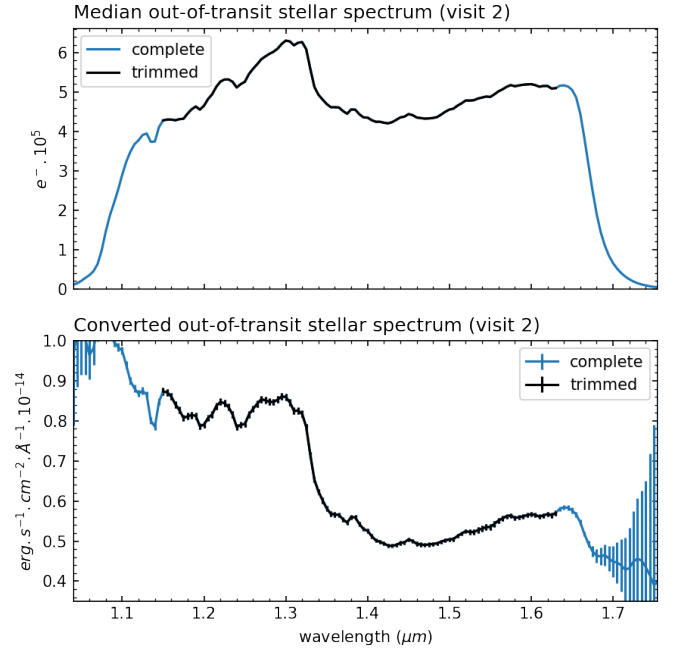


Fig. 4. Conversion of visit 2 out-of-transit stellar spectrum. The trimmed portion is used to perform the model fit.

Finally, we add to our dataset the Pan-STARRS g , r , i , and z photometry of TRAPPIST-1 (Chambers et al. 2016). These measurements were added to constrain the visible portion of the stellar spectrum, a choice motivated by the discrepancy observed when comparing the multi-component model from Wakeford et al. 2019 to these data (see Figure A.3).

4.3. Fitting the out-of-transit spectra

We fit the dataset previously described to Equation 4 for each visit individually, accounting for three distinct cases: a quiescent photosphere (1T), a photosphere with either spots or faculae (2T), and a photosphere with both spots and faculae (3T). For each visit and for each model, the best maximum a posteriori model parameters are found by following a brute force approach. This procedure consists of estimating the likelihood of the model

⁹ <https://hst-docs.stsci.edu/wfc3ihb/chapter-7-ir-imaging-with-wfc3/7-6-ir-optical-performance>

¹⁰ <http://www.stsci.edu/hst/instrumentation/wfc3/documentation/grism-resources/wfc3-g141-calibrations>

in a grid of discrete temperature combinations with 100 K steps (see Table 4). For each point in the grid, that is, for each temperature combination, the best covering fractions (between 0 and 1) are found using the BFGS optimization algorithm. This leads to a complete sampling of the likelihood function over all possible temperatures, and allows for exploration of the multi-modal nature of the likelihood distribution over the component temperatures. In this grid, the maximum likelihood parameters are retained, and refined with a parallelized Markov Chain Monte Carlo using *emcee* (Foreman-Mackey et al. 2013), this time in a continuous parameter space, from which we estimate their uncertainties (see subsection A.2). We find that the 2T model likelihood has a well-defined maximum (Figure A.8) while the 3T model is bimodal (see Figure A.10). Figure 5 shows the fitted out-of-transit spectrum for models 1T, 2T, and 3T, obtained by following this procedure on visit 1 data. As the theoretical stellar spectra are produced in 100K steps, we use this value as the uncertainty on the temperatures of the inferred components (see e.g., the temperature distributions in Figure A.10).

As in Wakeford et al. (2019), chi-squared statistics indicate that none of our models provide a good fit to the data from any visit. Moreover, the 1T model shows a larger discrepancy—which was also observed by Wakeford et al. (2019)—when modeling the HST/WFC3 TRAPPIST-1g out-of-transit spectrum against PHOENIX ACES models (Husser et al. 2013). In this latter study, this discrepancy is associated to a poor constraint on the stellar radius R_\star . This led the authors to introduce a scaling parameter to the stellar radius with the overall motivation being that it would account for the underestimation of the radii of low-mass stars by theoretical models. However, introducing such a factor not only would affect α but also the log surface gravity $\log_{10}(g) = GM_\star/R_\star^2$ involved in the stellar model parameters. Using such a radius scaling, varying the value of α and the log surface gravity provides a better fit to the data (see Figure A.4) but leads to $R_\star = 0.1134 \pm 0.0013 R_\odot$, which is different from the radius inferred by Agol et al. (2021) by $>3\sigma$. We decided not to consider this scaling in our study (we refer the interested reader to the analysis of Wakeford et al. (2019)) and instead use the unscaled radius found in Agol et al. (2021).

In order to understand the differences in the spectra obtained from the three visits, we plot the inferred temperatures and covering fractions found for each of them in Figure 6. Using the transmission spectrum correction described in the following section, we find that none of these models are able to explain the spectroscopic variability we observe. However, we note that only visit 1 contains the bottom of the transit signal and results in a transmission spectrum very similar to the one obtained through a joint analysis of all three visits. For this reason, we assume that the observed variability is not of astrophysical origin but is instead due to the partial coverage of two of the transits observed, combined with the systematic effects due to the instrument (see Figure A.5). With this conclusion, we assume that the photospheric structure of TRAPPIST-1 is consistent over the three visits and compare model Equation 4 to the median visits-combined out-of-transit spectrum, leading to the temperature components reported in Table 5 for the 1T, 2T, and 3T models. We notice that the hotter component of model 3T ($\sim 5000\text{K}$) corresponds to the maximum effective temperature in our model’s parameter space. Hence, this inferred temperature should be considered as a lower limit to the hot-spot temperature.

We note that the inferred 3T model, which includes bright spots covering a very small fraction of the stellar disk, is compatible (in order of magnitude) with the findings of Morris et al. (2018). In this latter study, the authors found that 32 ppm of

model	components	min-max (K)
1T	F_{phot}	1500-5000
2T	F_{spot}	1500-5000
	F_{phot}	1500-5000
3T	F_{spot}	1500-2300
	F_{phot}	2300-2700
	F_{fac}	2700-5000

Table 4. Temperature grids where covering fractions and model likelihoods are estimated, sampled in steps of 100K. The covering fractions for all components are allowed to vary from 0 to 1.

$5300 \pm 200\text{ K}$ bright spots are able to explain why the 3.3-day variability observed in the TRAPPIST-1 K2 light curve is undetectable in the *Spitzer* 4.5 μm band.

In order to compare our analysis to that of Wakeford et al. (2019), we repeat the modeling procedure described in this section using PHOENIX ACES models, which provides a poorer fit to the data. While the inferred stellar component temperatures are different from the ones found using the PHOENIX BT-Settl models, a bimodal likelihood distribution is also observed with these alternative models. For this reason, we base our study on the results presented in this section, which were obtained using the PHOENIX BT-Settle theoretical spectra.

4.4. Corrected transit depths

Using the models found in the previous section, the measured transmission spectra can now be corrected for the effect of stellar contamination. We apply corrections for five different configurations, corresponding to the 1T, 2T, and 3T models with the transit chords either passing completely over the base (F_{phot}) or the cooler (F_{spot}) portion of the photosphere. Due to its very small coverage, we do not consider a configuration where only the hotter component (F_{fac}) is occulted. Then, for each configuration and wavelength bin, the corrected transit depth can be expressed as:

$$\delta_c = \delta \times \frac{F}{F_{occ}}, \quad (5)$$

where δ is the measured transit depth, F_{occ} is the flux of the stellar disk occulted by the planet over the complete transit chord, and F is the overall flux of the stellar disk. As in Wakeford et al. (2019), we note that F_{occ} could be a linear combination of the flux components used to model the stellar disk. However, we decide to explore only the extreme cases where the occulted portion of the photosphere is made of a single temperature component. Applying this model to the five configurations outlined in Table 5 leads to the corrected transmission spectra plotted in Figure 7. Under the assumptions described above, these spectra should be of planetary origin, with the contribution from the star being modeled and corrected out. We denote the two-component and three-component photosphere models 2Tm and 3Tm, with the transit chord being over the 2600K and 2500K component, respectively. On the other hand, 2Tc and 3Tc correspond to transit configurations where the chord is over the cooler component of 2200K and 2000K, respectively. Finally, 1T denotes a quiescent photosphere at 2400K for which no spectrum correction is required.

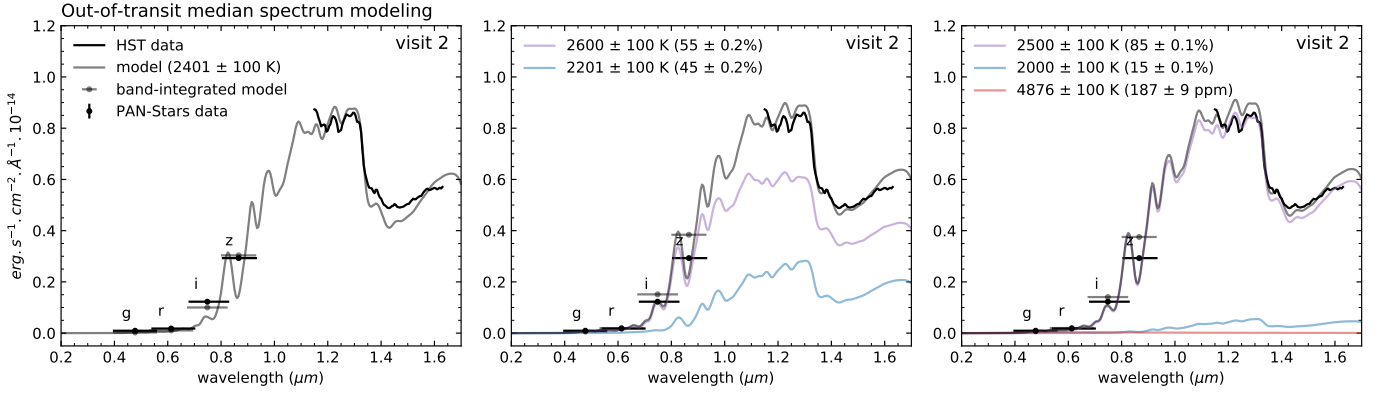


Fig. 5. *1T*, *2T*, and *3T* models of the visit 2 out-of-transit stellar spectrum.

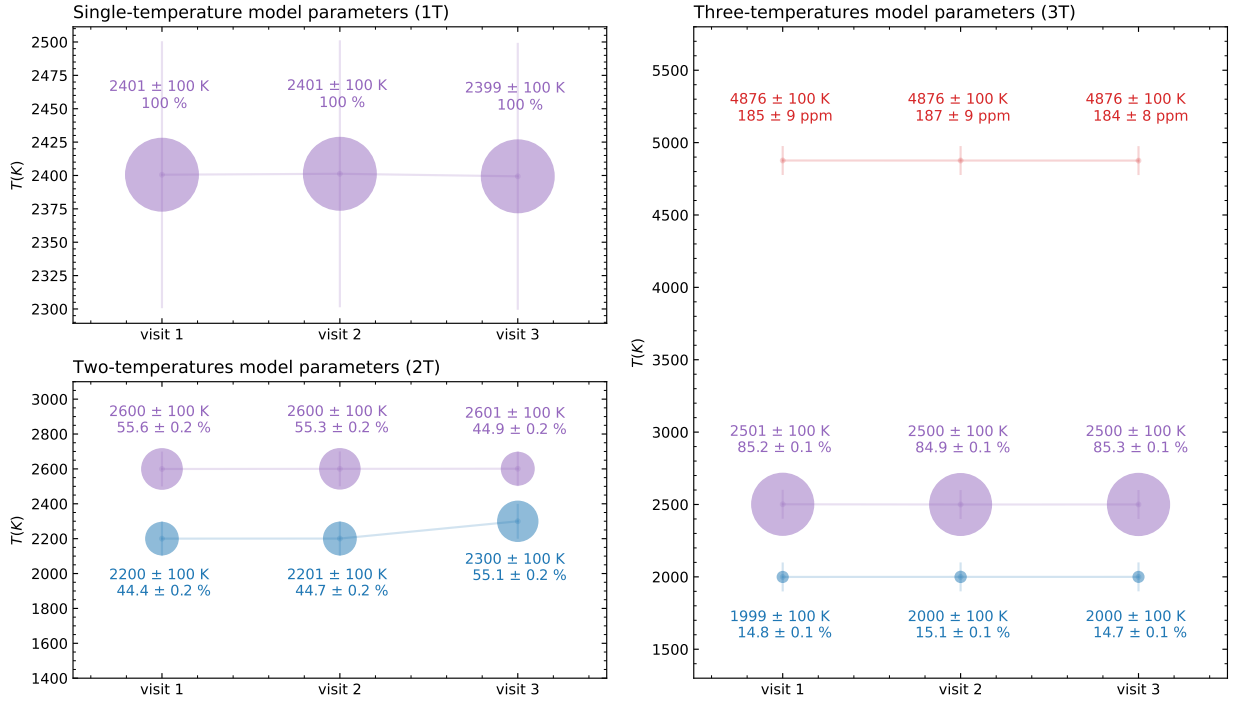


Fig. 6. Inferred temperatures and covering fraction for the *1T*, *2T*, and *3T* models on each visit.

model	covering fractions	temperatures	configuration
1T	100%	2400 ± 100 K	1T
2T	55.5 ± 0.1 %	2600 ± 100 K	2Tm
	44.5 ± 0.1 %	2200 ± 100 K	2Tc
3T	85.1 ± 0.1 %	2500 ± 100 K	3Tm
	14.9 ± 0.1 %	2000 ± 100 K	3Tc
	185.2 ± 8.8 ppm	4876 ± 100 K	3Th

Table 5. Multiple-temperature model parameters inferred from the visits-combined out-of-transit spectrum. For each of the *T1*, *T2*, and *T3* models, we consider a configuration where the stellar disk is occulted across a unique temperature component. The name of the configuration associated to each component is reported in the last column.

5. Planetary spectrum

In this section, we use the plausible stellar photospheric models from the previous sections to guide our planetary atmospheric

models and interpret the planetary transmission spectra. Our primary aim here is to use the potential planetary and stellar scenarios together to find the most likely scenario for each. In so doing, we (1) rule out possible end-member photospheric configurations in cases where they require transmission spectra without a plausible atmospheric model and (2) rule out potential planetary atmospheric conditions when none of the possible transmission spectra (given the allowed photospheric configurations) are well fitted by an atmospheric model. We summarize the results of the allowable stellar photospheric configurations given the planetary models in Table 6 and the possible planetary models given the data in Table 7.

5.1. Transmission forward models

Once we had generated all transit spectrum scenarios (1T, 2Tc, 2Tm, 3Tc, 3Tm, and 3Th), we computed model atmospheric spectra for TRAPPIST-1 h against which we were able to com-

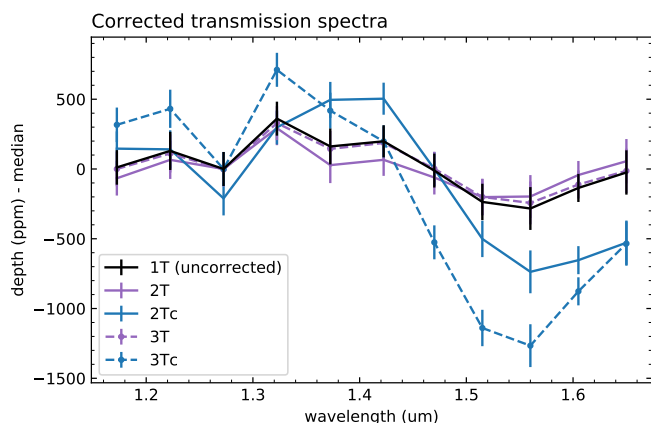


Fig. 7. Corrected transmission spectra under the five configurations reported in Table 5. Colored solid lines correspond to the two-temperature models (2T) and dotted lines denote the three-temperature models (3T). Purple lines represent spectra of planet h transiting the quiescent component of the stellar photosphere (2T and 3T) while blue lines indicate spectra of planet h transiting the cooler component of the stellar photosphere (2Tc and 3Tc).

pare the data. We did not run models to compare against scenario 3Th, as the hot spot component is too small to be entirely transited by the planet. As in Wakeford et al. (2019), we used the forward modeling capabilities of the one-dimensional radiative transfer code CHIMERA (Line et al. 2013), as has previously been modified for the inner TRAPPIST-1 planets (Batalha et al. 2018; Moran et al. 2018). CHIMERA uses the correlated- k method for radiative transfer and the five-parameter, double, gray, one-dimensional temperature-pressure profile of Guillot (2010). We run models in chemical equilibrium, which draw from a pre-computed grid at each temperature and metallicity bin, where we consider a temperature of 170 K and metallicities of between 1 and 1000 times solar. While we include Rayleigh scattering due to H_2/He , we neglect any further scattering or absorption from clouds or hazes explicitly. Given the precision of our observations, we always first consider the simplest aerosol-free atmospheric models in exploring possible atmospheric signatures. For each model atmosphere, we use a planetary mass of $0.755 M_\oplus$ and a solid body radius of $0.326 R_\oplus$, as determined by Agol et al. (2021).

Because the planetary equilibrium temperature is very cold, namely ~ 170 K, the atmospheric scale height H even for a solar metallicity (2.32μ) atmosphere is quite small despite the low gravity of the planet (5.6 ms^{-2} , Agol et al. 2021), with $H \sim 100$ km. For reference, H in an N_2 atmosphere (28μ) for TRAPPIST-1 h would be ~ 9 km. For our solar-metallicity model atmosphere, we include opacities from water, methane, carbon monoxide, carbon dioxide, ammonia, molecular nitrogen, and H_2/He collision-induced-absorption (CIA) (Freedman et al. 2008, 2014). For the water- and methane-rich ten-times-solar atmosphere, we include only water, methane, and H_2 -CIA in order to produce the largest molecular features in the WFC3 G141 bandpass. These larger features result from the water and methane abundance increasing before the mean molecular weight increases enough to sufficiently shrink the atmospheric scale height (Kempton et al. 2017; Moran et al. 2018). Given the relatively flat transit spectrum scenarios of the data, we explicitly model this water- and methane-rich ten-times-solar atmosphere because it is the least likely model to fit the observed data; though we note that for most planetary transit depths, this is

still rejected at less than 3σ . Additionally, we model a CO_2 -rich atmosphere at 200 times solar, including opacities from CO_2 , CH_4 , and CO .

Finally, we also model a pure N_2 atmosphere without Rayleigh scattering, which in the near-infrared (NIR) region of WFC3 G141 is also representative of an airless body, as well as potentially representing a heavily aerosol-laden atmosphere. Moran et al. (2018) showed that, for the inner TRAPPIST-1 planets, aerosols cannot produce a flat line transmission spectrum in the HST WFC3 G141 band in a low mean molecular weight atmosphere. However, the precision of the WFC3 G141 data combined with TRAPPIST-1h’s small scale height is such that we cannot rule out aerosols as a potential fit to the data here. Though this “flat line” scenario fits the data best (i.e., it produced the lowest reduced- χ^2 value), we cannot completely discount any of the modeled spectra to high significance given the data.

5.2. Model results with HST

In Figure 8, we show the results of our three modeled atmospheres for TRAPPIST-1 h compared to all five considered transit spectrum scenarios. In our figures, we show the data and models normalized by the mean of the flat model for better comparison. For scenarios 2Tc and 3Tc, we can rule out a solar metallicity H/He -dominated atmosphere at 4.5σ and 6σ , respectively, where these σ values are calculated from the critical values of our χ^2_ν for the data and the models. The water- and methane-rich atmosphere model excludes the 2Tc and 3Tc scenarios to greater than 5σ . While we cannot rule out the flat line model against the 2Tc/3Tc scenarios at $\geq 3\sigma$ with the HST data alone, we can reject these potential spectra with relative confidence using the extended wavelength coverage of Spitzer, K2, and ground-based data, discussed further below.

The remaining transit depth scenarios—1T, 2Tm, and 3Tm—fit to better than 3σ for each atmosphere, limiting our ability to confidently discount a particular transit depth scenario or atmospheric model. However, with the HST WFC3 data, we can rule out the ten times solar, water- and methane-rich atmosphere to nearly 2.5σ for each of the transit depth scenarios and the 1 times solar metallicity to nearly 2σ . However, in each case, we minimize our χ^2 with the N_2 atmosphereless or airless body, aerosol-laden model. For 1T, 2Tm, and 3Tm, these values are $\chi^2_\nu = 1.9, 0.9$, and 1.5 , respectively, where $\chi^2_\nu = \chi^2/\nu$ with $\nu = 12$. Given a random draw of data from the model with the same uncertainty and resolution, one would get a model that would fit the data better 97.05%, 45.39%, and 88.43% of the time for the 1T, 2Tm, and 3Tm scenarios, respectively. This is the χ^2 cumulative distribution function (CDF), where values between 16% and 84% represent the 1σ residual distribution (Wilson 2021). We report the χ^2 CDF along with our χ^2_ν values throughout the rest of the analysis.

5.3. Model results with full wavelength coverage

In Figure 9, we show the results of the previously modeled planetary atmospheres ($1\times$ and $10\times$ solar metallicity and a “flat” model) in addition to a carbon dioxide-rich, 200 times solar metallicity atmosphere compared to an extended wavelength range from $0.8 \mu\text{m}$ to $4.5 \mu\text{m}$ of all existing transits of TRAPPIST-1 h. We include both the HST WFC3 G141 spectroscopic data analyzed here and additional photometric data from the space-based K2 campaign (Grimm et al. 2018), the SPECULOOS-South Observatory (SSO) and the Liverpool Tele-

Photospheric configuration	Plausible?	Explanation
1T	Yes	Cannot be ruled out beyond 1.4σ with any atmospheric model
2Tm	Yes	Cannot be ruled out beyond 1σ with any atmospheric model
2Tc	Unlikely	Can be ruled out beyond 3.5σ with any H_2 -rich model; Can be ruled out to $\sim 1\sigma$ with flat model
3Tm	Yes	Cannot be ruled out beyond 1.3σ with any atmospheric model
3Tc	No	Can be ruled out beyond 2.5σ with every atmospheric model
3Th	No	Hot spot coverage too small for planet to transit

Table 6. Summary of which stellar photospheric configurations remain plausible when including the interpretation of planetary atmospheric models.

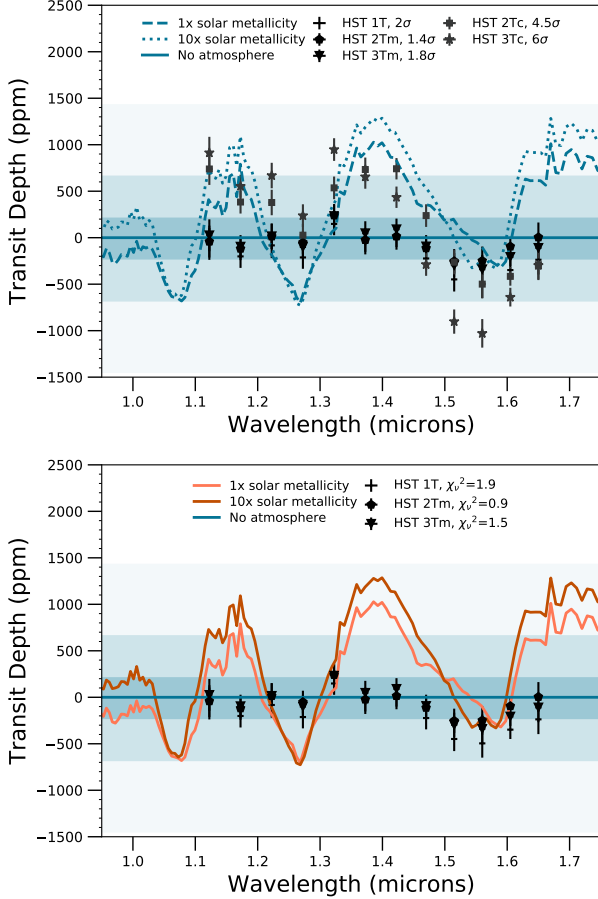


Fig. 8. Our considered model atmospheres produced using CHIMERA compared to the five potential planetary spectrum scenarios. TOP: In addition to the mean-subtracted models (solid, dashed, and dotted lines), we include 1σ , 2σ , and 3σ errors of the flat “no atmosphere” model as blue shaded regions. The confidence to which the solar metallicity scenario can be ruled out is reported after each scenario. The cold spot scenarios, 3Tc and 2Tc, can be clearly ruled out at high confidence. Of the remaining models and scenarios, no model can be confidently excluded at $\geq 3\sigma$. However, a featureless infrared spectrum (solid line) either due to an airless body or an atmosphere without infrared features (e.g., a molecular nitrogen atmosphere) is statistically preferred over a 1 times solar metallicity atmosphere (dashed line) or a ten times solar, water- and methane-rich atmosphere (dotted line). BOTTOM: Scenarios with the best goodness of fit (1T, 2Tm, 3Tm) against the three model atmospheres ($1\times$ solar, light orange; $10\times$ solar, dark orange; no atmosphere, blue). We report the χ^2_ν of the flat line after the three scenarios in the legend.

scope (LT) on the ground (Ducrot et al. 2018), and Spitzer/IRAC data at $3.6\ \mu\text{m}$ and $4.5\ \mu\text{m}$ (Ducrot et al. 2020). We use the

Spitzer transit depths reported by Ducrot et al. (2020) in their Table 6, as these represent the depths of their global analysis. These data are therefore subject to fewer systematic errors between the two channels, in addition to being the preferred results by Ducrot et al. (2020). We then multiply these measured transit depths by the appropriate correction factor for each stellar configuration, as performed for the Spitzer $4.5\ \mu\text{m}$ point in Wakeford et al. (2019).

Because of the potentially different systematic errors between the HST observations and those of the other telescope data (e.g., de Wit et al. 2016, 2018; Ducrot et al. 2020), we include various offsets for the transit depths for the Spitzer, K2, SSO, and LT data points. We allow these data to float within the range defined by their 1σ errors and choose the offset that produces the minimum χ^2 with the HST data after the appropriate correction factor is applied for each stellar photosphere scenario. Therefore, from the values given in Ducrot et al. 2020, the K2 point was allowed to float ± 580 ppm, the LT point ± 350 ppm, the SSO point ± 360 ppm, and the Spitzer points ± 210 ppm. We marginalize over the offset that favors the flattening of the K2, SSO, and LT data, as the large offsets between these measurements as reported by Ducrot et al. (2018) require an unphysically large scattering slope in the NIR (e.g., Moran et al. 2018). As discussed below, the fact that relatively few transits were measured by K2, SSO, and LT (1, 3, and 1, respectively; Ducrot et al. 2018) means that the associated error may also be higher than reported; however, these data do not ultimately guarantee the validity of or rule out any of the atmospheric models, given their already low precisions relative to the HST data. We treat the K2, SSO, and LT data as separate independent floats, but we treat the two Spitzer points together, using the larger error from the $3.6\ \mu\text{m}$ data point as the allowable offset.

We note that the preferred offset for the Spitzer points is the upper limit of how far we allow it to float, perhaps suggesting an underestimation of the overall error assumed across our measurements. However, for consistency, we maintain the 1σ error as the allowable offset range. In an effort to generate a potential atmosphere with molecular features that approach the transit depth of the $4.5\ \mu\text{m}$ Spitzer point, we included the 200 times solar CO_2 -rich atmosphere, where the presence of carbon monoxide produces a spectral feature in this range. We discuss if such an atmosphere is physically realistic in subsection 5.4.

As stated above, the addition of the increased wavelength coverage allows us to fully discard the scenario 3Tc for the stellar photosphere. All atmospheric models are ruled out to well over 5σ for 3Tc, except for the flat model, which is ruled out to 2.5σ , and the 200 times solar carbon-rich model, which is ruled out to 2.9σ . For scenario 2Tc, we can confidently exclude all but the flat and carbon-rich atmospheres, though we do increase our ability to reject the fit for 2Tc from less than 1σ (0.7σ) with HST data alone to nearly 1σ (0.9σ) with the full wavelength

coverage. While not fully ruled out, we nevertheless choose not to include scenario 2Tc in Figure 9 as it is the least preferred of the remaining stellar photospheric scenarios.

For the remaining stellar photospheres (1T, 2Tm, and 3Tm), the addition of the wider wavelength coverage does not allow us to rule out any atmospheric scenario with high confidence. For the one times solar metallicity atmosphere, we can only rule out scenario 2Tm to 0.5σ and scenarios 3Tm and 1T to 0.6σ and 0.7σ , respectively. For the water-rich ten times solar atmosphere, we can rule out transit depth scenarios 1T, 2Tm, and 3Tm to between 1.1 and 1.4σ . Both the 200 times solar atmosphere and the featureless “flat”/N₂ atmosphere models provide the best minimized χ^2 fits to the remaining data. However, the flat model is slightly preferred over the carbon-dioxide-rich model. For scenarios 1T, 2Tm, and 3Tm, the carbon-dioxide-rich atmosphere results in $\chi^2_{\nu} = 4.0, 3.3$, and 3.7 . Using the χ^2 CDF allows us to rule these out entirely, with a better dataset being drawn from the model 100% of the time (Wilson 2021). The flat model results in $\chi^2_{\nu} = 1.4, 1.0$, and 1.1 , with 17 degrees of freedom (χ^2 CDF of 87.50%, 54.56%, and 65.40%) compared to scenarios 1T, 2Tm, and 3Tm. As in Wakeford et al. (2019), this suggests the best fitting or “preferred” stellar photospheric model is 3Tm, though we stress that we cannot actually constrain the stellar photosphere to high confidence with these existing measurements.

5.4. Implications of planetary atmospheric models

In constructing our planetary atmospheric models, we in part sought to maximize the potential differences between models to see if we could tell them apart based on the HST and additional wavelength data. While we cannot do so at high statistical significance, we ultimately determine that all evidence points to TRAPPIST-1 h having a high-mean-molecular-weight atmosphere ($\geq 1000\times$ solar metallicity), a highly opaque aerosol layer, or no atmosphere, which cannot be distinguished with the current data precision.

The remaining models we show in Figure 8 and Figure 9 vary in terms of being physically realistic, which we explore here. The $1\times$ and $10\times$ solar metallicity model atmospheres are hydrogen-dominated. Such light atmospheres are most prone to atmospheric escape, though the location of TRAPPIST-1 h, that is, farthest from the star, in principle means it is also most likely to have retained such an atmosphere against both hydrodynamic escape or via water photolysis, depending on its initial orbit and evolution (e.g., Bolmont et al. 2017; Bourrier et al. 2017). However, given the age of the TRAPPIST-1 system (~ 7 Gyr; Burgasser & Mamajek 2017), it is unlikely even for TRAPPIST-1 h to have retained a hydrogen-dominated atmosphere up until the present day, as it would lose the necessary hydrogen envelope to fit the mass–radius relationship given a terrestrial core in less than 100 Myr (Turbet et al. 2020a). Furthermore, Turbet et al. (2020a) argue that, given the total H-containing volatiles that any of the planets can accrete (Hori & Ogihara 2020), any individual planet that accreted a larger fraction would result in a markedly different density from the others, but instead very similar densities are observed for all the planets in the TRAPPIST-1 system (Grimm et al. 2018; Agol et al. 2021). Therefore, given our poor (though not statistically excluded) fits to the data with the hydrogen-dominated atmospheric models, combined with these theoretical concerns, we can conclude that TRAPPIST-1 h is highly unlikely to have a hydrogen-dominated atmosphere.

Given the size of the planet, which is between that of Mars and Earth, as well as its equilibrium temperature on the colder edge of that of Mars, we considered a 200 times solar metal-

licity, CO₂-rich atmosphere. However, at this cold a temperature (~ 170 K) and metallicity, both water and carbon dioxide are near the point where they can condense out of the atmosphere as crystalline ice clouds, or are vulnerable to atmospheric collapse entirely (Turbet et al. 2018). Only very thick CO₂ atmospheres would be stable against collapse (Lincowski et al. 2018; Turbet et al. 2018), unless significant inventories of H₂ or CH₄ were present (Ramirez & Kaltenegger 2017; Turbet et al. 2020b). This is similar to our naive 200 times solar CO₂-rich atmosphere. To demonstrate the unlikelihood of these CO₂ scenarios fitting the existing HST, Spitzer, and short-wavelength data, we calculate the absolute difference in transit depth between the Ch. 1 and Ch. 2 Spitzer points, which is approximately 350 ppm. For a pure CO₂ atmosphere (44μ), this corresponds to 50 scale heights (H), which is an unrealistically large extent for the planet. For our 200 times solar atmosphere with a mean molecular weight of $\sim 5\mu$, the difference in transit depths is 5H, which while large is not beyond the realm of possibility from theory (e.g., Miller-Ricci et al. 2009). Still, we cannot compellingly explain the Spitzer 4.5μ with plausible models, despite not being able to rule them out statistically with the current data precision. Instead, a very high mean molecular weight atmosphere ($\geq 1000\times$ solar metallicity) or no atmosphere at all remain the best explanations of the existing data, though we cannot tell these potential atmospheres (or lack thereof) apart at present.

Future observations are necessary to provide the higher precision and wavelength coverage needed to truly understand the existence and contents of an atmosphere around TRAPPIST-1 h. Furthermore, such higher quality data and wavelength coverage would allow future retrieval studies to place stronger quantitative constraints on the planet (e.g., Barstow & Heng 2020). As part of General Observer Cycle 1, the JWST NIRSpec/PRISM will observe three transits of the planet from 0.6 to 5.3μ (JWST GO 1981; PIs Stevenson and Lustig-Yaeger), which will negate the need for offsets such as those calculated here, and will provide sufficient precision to distinguish between various high-metallicity atmospheres containing water, carbon dioxide, nitrogen, carbon monoxide, and methane. These observations, along with the atmospheric retrievals they enable, can also offer further insight into the potential condensate clouds of TRAPPIST-1 h, constraints on which are beyond the precision of the existing HST, K2, SSO, LT, or Spitzer data.

5.5. Planetary model summary

In summary, we find that we can make several determinations about the nature of the star TRAPPIST-1 and the planet TRAPPIST-1 h using the combination of atmospheric models and potential stellar photospheres. We can fully discount photospheric configuration 3Th and 3Tc and tentatively discount scenario 2Tc. The remaining scenarios – 1T, 2Tm, and 3Tm – all produce reasonable transmission spectra to which we can fit atmospheric models, as summarized in Table 6. For the planetary atmosphere, we can draw no strongly statistically significant conclusions based on the data; however, we do find some atmospheric models fit better than others for the allowable stellar configurations. While H₂-rich atmospheres cannot be ruled out to greater than 3σ , they show much poorer fits to the existing data from HST, even with the expanded wavelength coverage offered by K2, SSO, LT, and Spitzer. In all cases, a flat model representing either no atmosphere or a very high mean molecular weight atmosphere ($\geq 1000\times$ solar metallicity) provide the best fit χ^2 s. These findings are also summarized in Table 7.

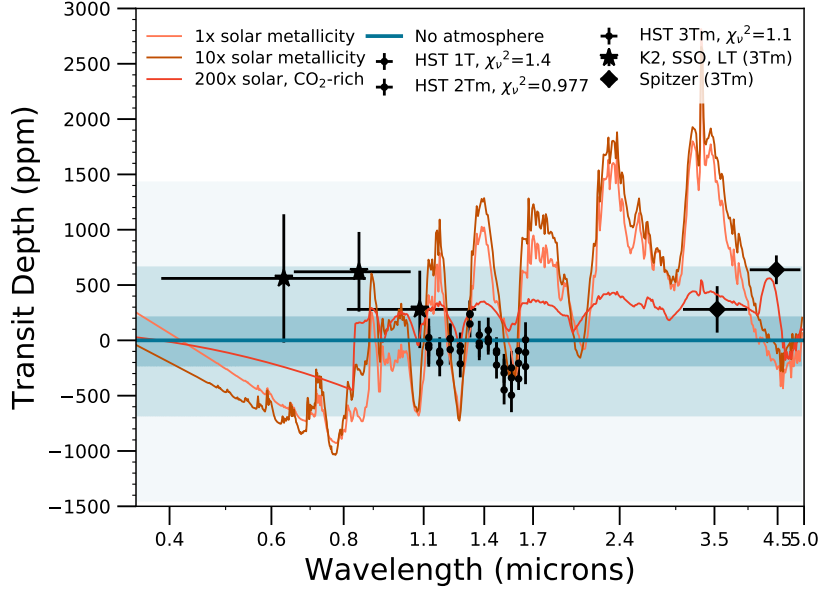


Fig. 9. As in Figure 8 (bottom) with the addition of K2/SSO/LT data points (Ducrot et al. 2018) and Spitzer IRAC Ch. 1 and Ch. 2 data (Ducrot et al. 2020), shown here corrected for stellar contamination scenario 3Tm, the “best-fit” configuration. We also include our carbon-dioxide-rich atmospheric model to compare against the data, though in all scenarios for the stellar photosphere, we minimize the χ^2 with the flat “high mean molecular weight/no atmosphere” model, which we report as χ^2_v after each transit depth scenario in the legend. We note that we have applied offsets to the K2, SSO, LT, and Spitzer data, as discussed in the text.

Planetary atmosphere	Description	Plausible?	Explanation
1× solar	Chemical equilibrium Rayleigh scattering H_2 , He, H_2O , CH_4 , CO, CO_2 , NH_3 , N_2	Strongly unlikely	Poor fit to data, though not ruled out to 1σ
10× solar	Chemical equilibrium Rayleigh scattering H_2 , H_2O , CH_4	Strongly unlikely	Poor fit to data, but only ruled out to 1σ
200× solar	Chemical equilibrium Rayleigh scattering CH_4 , CO, CO_2	Unlikely	Fits data with χ^2_v of ~ 4 or better
No atmosphere/ Flat model/ Heavily aerosol-laden	No Rayleigh scattering N_2	Yes	Fits data with χ^2_v of ~ 1.4 or better

Table 7. Summary of atmospheric models considered and their plausibility given the data

6. Conclusion

We present an analysis of the infrared transmission spectrum of TRAPPIST-1h, from 1.12 to 1.65 μm , obtained with the HST Wide Field Camera 3 and using the G141 grism. The spectra were extracted from the raw images with a pipeline based on the prose framework, and the resulting spectroscopic light curves modeled within a Bayesian framework, with a systematic error model selected through the minimization of the AIC. In order to disentangle the planetary spectrum from the stellar one (addressing the so-called stellar contamination effect), we modeled the median out-of-transit spectrum of TRAPPIST-1 against a multi-temperature combination of the PHOENIX BT-Settl theoretical models, following the approach of Wakeford et al. (2019). While the retrieved transmission spectra from each individual visit vary, none of our single-, two-, or three-component photospheric models (each component having a different temperature) is able to explain this variability. Nevertheless, our three-component model suggests the possibility that TRAPPIST-1 sur-

face may be covered by $14.9\% \pm 0.1\%$ of cold spots ($2000K \pm 100K$) and by a very small fraction (185.2 ± 8.8 ppm) of hot spots (hotter than 5000K). This result is compatible with the results of Morris et al. (2018), explaining the varying amplitude of the photometric variability of TRAPPIST-1 observed between K2 and Spitzer. However, we find that none of our photosphere models, including a homogeneous photosphere, provide a good fit to the data. While it might come from the accuracy of the PHOENIX models being used, our approach requires constraints on the photospheric structure of TRAPPIST-1 in order to break the multiple degeneracies encountered when fitting multi-component models to the data. This prior knowledge is not yet available for ultra-cool dwarf stars, but will certainly be essential for the atmospheric characterizations to come. To this end, tools like the ensemble analysis methodology described in Luger et al. (2021), or transmission spectroscopy of active region occultations (Espinoza et al. 2019) offer promising avenues. Finally, we draw particular attention to the very simplistic nature of the active region modeling used in section 4, which is foreseen to be

improved by further study of ultra-cool dwarf star photospheres as these objects are particularly valuable to the study of small exoplanets.

With the potential stellar photospheric scenarios in hand, we modeled a number of different planetary atmospheres using the forward model CHIMERA, including various H₂-dominated atmospheres, a carbon-dioxide-rich atmosphere, and a featureless “flat” line model. While the data quality combined with the cold, small (likely rocky) nature of the planet are not sufficient to exclude any atmospheric scenario to high statistical significance, we conclude that TRAPPIST-1 h is highly unlikely to possess a hydrogen-dominated atmosphere (a conclusion independently reached by Gressier et al. 2022). The likeliest scenario for this planet is that it possesses a very high mean molecular weight ($\geq 1000\times$ solar metallicity) atmosphere, is enshrouded by an opaque aerosol layer, or is devoid of atmosphere entirely. Determination of the true nature of the atmosphere of TRAPPIST-1 h, or lack thereof, awaits upcoming measurements by JWST.

7. Acknowledgment

This research made use of exoplanet (Foreman-Mackey et al. 2021) and its dependencies (Agol et al. 2020; Kumar et al. 2019; Astropy Collaboration et al. 2013, 2018; Foreman-Mackey et al. 2020; Luger et al. 2019; Salvatier et al. 2016b; Theano Development Team 2016). We acknowledge support from the BELSPO program BRAIN-be 2.0 (Belgian Research Action through Interdisciplinary Networks) contract B2/212/B1/PORTAL. This publication benefits from the support of the French Community of Belgium in the context of the FRIA Doctoral Grant awarded to L.J.G. MG is F.R.S.-FNRS Senior Research Associate. B.V.R. thanks the Heising-Simons Foundation for support. S.E.M. acknowledges support from NASA Earth and Space Science Fellowship grant 80NSSC18K1109. Finally, this work is based on observations made with the NASA/ESA Hubble Space Telescope that were obtained at the Space Telescope Science Institute, which is operated by the Association of Universities for Research in Astronomy, Inc. These observations are associated with programs and grants under GO-15304 (PI. J. deWit)

References

Agol, E., Dorn, C., Grimm, S. L., et al. 2021, Refining the transit timing and photometric analysis of TRAPPIST-1: Masses, radii, densities, dynamics, and ephemerides

Agol, E., Luger, R., & Foreman-Mackey, D. 2020, *AJ*, 159, 123

Akaike, H. 1974, *IEEE Transactions on Automatic Control*, 19, 716

Allard, F., Homeier, D., & Freytag, B. 2012, *Philosophical Transactions of the Royal Society of London Series A*, 370, 2765

Apai, D., Rackham, B. V., Giampapa, M. S., et al. 2018, *arXiv e-prints*, arXiv:1803.08708

Astropy Collaboration, Price-Whelan, A. M., Sipőcz, B. M., et al. 2018, *AJ*, 156, 123

Astropy Collaboration, Robitaille, T. P., Tollerud, E. J., et al. 2013, *A&A*, 558, A33

Barstow, J. K. & Heng, K. 2020, *Space Sci. Rev.*, 216, 82

Batalha, N. E., Lewis, N. K., Line, M. R., Valenti, J., & Stevenson, K. 2018, *ApJ*, 856, L34

Bolmont, E., Selsis, F., Owen, J. E., et al. 2017, *MNRAS*, 464, 3728

Bourque, M., Espinoza, N., Filippazzo, J., et al. 2021, *The Exoplanet Characterization Toolkit (ExoCTK)*

Bourrier, V., de Wit, J., Bolmont, E., et al. 2017, *AJ*, 154, 121

Burgasser, A. J. & Mamajek, E. E. 2017, *ApJ*, 845, 110

Chambers, K. C., Magnier, E. A., Metcalfe, N., et al. 2016, *arXiv e-prints*, arXiv:1612.05560

Charbonneau, D. 2009, in *Transiting Planets*, ed. F. Pont, D. Sasselov, & M. J. Holman, Vol. 253, 1–8

Charbonneau, D., Brown, T. M., Noyes, R. W., & Gilliland, R. L. 2002, *ApJ*, 568, 377

de Wit, J., Wakeford, H. R., Gillon, M., et al. 2016, *Nature*, 537, 69

de Wit, J., Wakeford, H. R., Lewis, N. K., et al. 2018, *Nature Astronomy*, 2, 214

Deming, D., Wilkins, A., McCullough, P., et al. 2013, *ApJ*, 774, 95

Ducrot, E., Gillon, M., Delrez, L., et al. 2020, *A&A*, 640, A112

Ducrot, E., Sestovic, M., Morris, B. M., et al. 2018, *AJ*, 156, 218

Espinoza, N., Rackham, B. V., Jordán, A., et al. 2019, *MNRAS*, 482, 2065

Foreman-Mackey, D., Hogg, D. W., Lang, D., & Goodman, J. 2013, *PASP*, 125, 306

Foreman-Mackey, D., Luger, R., Agol, E., et al. 2021, *The Journal of Open Source Software*, 6, 3285

Foreman-Mackey, D., Luger, R., Czekala, I., et al. 2020, *exoplanet-dev/exoplanet* v0.4.3

Freedman, R. S., Lustig-Yaeger, J., Fortney, J. J., et al. 2014, *ApJS*, 214, 25

Freedman, R. S., Marley, M. S., & Lodders, K. 2008, *ApJS*, 174, 504

Gaia Collaboration, Brown, A. G. A., Vallenari, A., et al. 2018, *A&A*, 616, A1

Gillon, M., Triaud, A. H. M. J., Demory, B.-O., et al. 2017, *Nature*, 542, 456

Gressier, A., Mori, M., Changeat, Q., et al. 2022, *A&A*, 658, A133

Grimm, S. L., Demory, B.-O., Gillon, M., et al. 2018, *A&A*, 613, A68

Guillot, T. 2010, *A&A*, 520, A27

Head, J. D. & Zerner, M. C. 1985, *Chemical Physics Letters*, 122, 264

Hori, Y. & Ogihara, M. 2020, *ApJ*, 889, 77

Horne, K. 1986, *PASP*, 98, 609

Husser, T. O., Wende-von Berg, S., Dreizler, S., et al. 2013, *A&A*, 553, A6

Kempton, E. M. R., Lupu, R., Owusu-Asare, A., Slough, P., & Cale, B. 2017, *PASP*, 129, 044402

Kreidberg, L., Bean, J. L., Désert, J.-M., et al. 2014, *Nature*, 505, 69

Kumar, R., Carroll, C., Hartikainen, A., & Martin, O. A. 2019, *The Journal of Open Source Software*

Kuntzschner, H., Kümmel, M., Walsh, J. R., & Bushouse, H. 2011, *Revised Flux Calibration of the WFC3 G102 and G141 grisms*, Space Telescope WFC Instrument Science Report

Lincowski, A. P., Meadows, V. S., Crisp, D., et al. 2018, *ApJ*, 867, 76

Line, M. R., Wolf, A. S., Zhang, X., et al. 2013, *ApJ*, 775, 137

Luger, R., Agol, E., Foreman-Mackey, D., et al. 2019, *The Astronomical Journal*, 157, 64

Luger, R., Agol, E., Foreman-Mackey, D., et al. 2019, *AJ*, 157, 64

Luger, R., Foreman-Mackey, D., & Hedges, C. 2021, *arXiv e-prints*, arXiv:2102.01697

Luger, R., Sestovic, M., Kruse, E., et al. 2017, *Nature Astronomy*, 1, 0129

Lustig-Yaeger, J., Meadows, V. S., & Lincowski, A. P. 2019, *AJ*, 158, 27

Miller-Ricci, E., Seager, S., & Sasselov, D. 2009, *ApJ*, 690, 1056

Moran, S. E., Hörst, S. M., Batalha, N. E., Lewis, N. K., & Wakeford, H. R. 2018, *AJ*, 156, 252

Morley, C. V., Kreidberg, L., Rustamkulov, Z., Robinson, T., & Fortney, J. J. 2017, *ApJ*, 850, 121

Morris, B. M., Agol, E., Davenport, J. R. A., & Hawley, S. L. 2018, *ApJ*, 857, 39

Pirzkal, N., Ryan, R., & Brammer, G. 2016, *Trace and Wavelength Calibrations of the WFC3 G102 and G141 IR Grisms*, Space Telescope WFC Instrument Science Report

Pont, F., Knutson, H., Gilliland, R. L., Moutou, C., & Charbonneau, D. 2008, *MNRAS*, 385, 109

Rackham, B., Pinhas, A., Apai, D., et al. 2019a, *BAAS*, 51, 328

Rackham, B. V., Apai, D., & Giampapa, M. S. 2018, *ApJ*, 853, 122

Rackham, B. V., Apai, D., & Giampapa, M. S. 2019b, *AJ*, 157, 96

Ramirez, R. M. & Kaltenegger, L. 2017, *ApJ*, 837, L4

Salvatier, J., Wiecki, T. V., & Fonnesbeck, C. 2016a, *PeerJ Computer Science*, 2, e55

Salvatier, J., Wiecki, T. V., & Fonnesbeck, C. 2016b, *PeerJ Computer Science*, 2, e55

Theano Development Team. 2016, *arXiv e-prints*, abs/1605.02688

Tsiaras, A., Waldmann, I. P., Rocchetto, M., et al. 2016, *ApJ*, 832, 202

Turbet, M., Bolmont, E., Bourrier, V., et al. 2020a, *Space Sci. Rev.*, 216, 100

Turbet, M., Bolmont, E., Leconte, J., et al. 2018, *A&A*, 612, A86

Turbet, M., Boulet, C., & Karman, T. 2020b, *Icarus*, 346, 113762

Van Grootel, V., Fernandes, C. S., Gillon, M., et al. 2018, *ApJ*, 853, 30

Wakeford, H. R., Lewis, N. K., Fowler, J., et al. 2019, *AJ*, 157, 11

Wakeford, H. R., Sing, D. K., Evans, T., Deming, D., & Mandell, A. 2016, *ApJ*, 819, 10

Wilson, T. J. 2021, *Research Notes of the American Astronomical Society*, 5, 265

Appendix A: Complementary figures

A.1. Spectra extraction and modeling comparison

A.2. Out-of-transit spectra inference

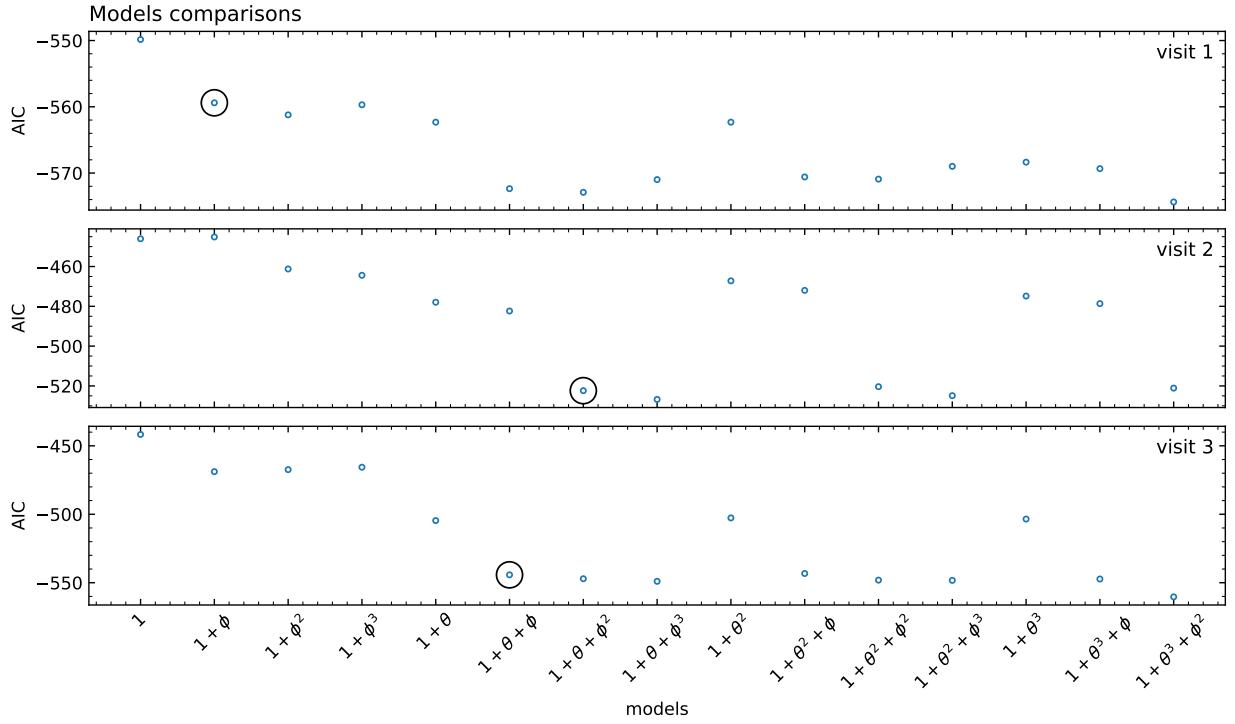


Fig. A.1. Model comparison for visits 1, 2, and 3. The x-axis represents the systematic error model where 1 designates a constant, θ^n a polynomial order n of θ , and ϕ^m a polynomial order m of ϕ . The best model is circled. For one model to be considered better than another, we require that the AIC difference between it and the others be greater than 20.

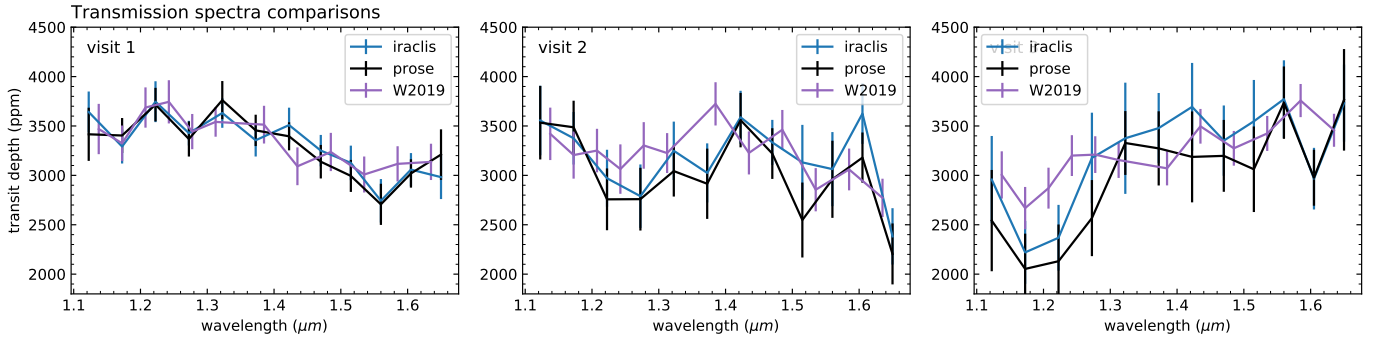


Fig. A.2. Comparison of the transmission spectra of our three HST visits obtained with iraclis, prose, and the method from Wakeford et al. (2019). The larger discrepancy of visit 3 for the method of Wakeford et al. (2019) (especially between 1.1 and 1.3 μm) is due to the partial masking of the first orbit, whereas the other two analyses discard it.

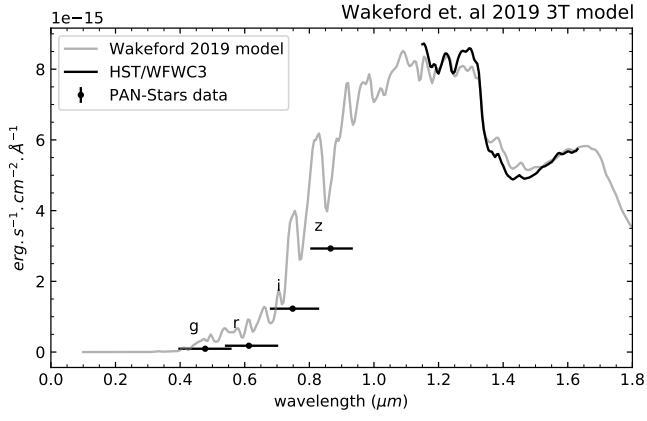


Fig. A.3. Wakeford et al. 2019 three-component model against our HST data and Pan-STARRS g, r, i, and z wide-band photometry

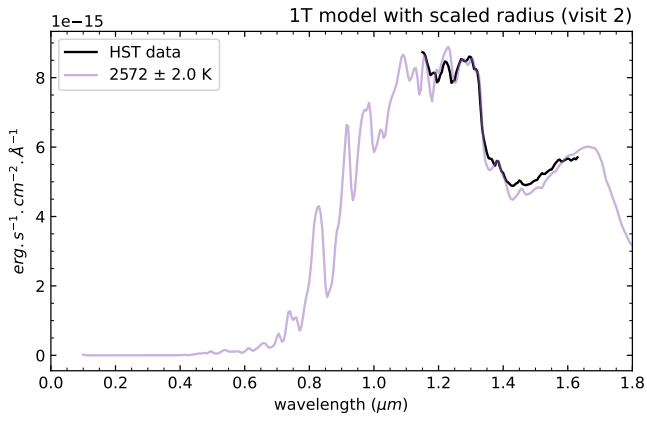


Fig. A.4. Visit 2 single-component photospheric model, allowing for a scaled radius (as in Wakeford et al. 2019)

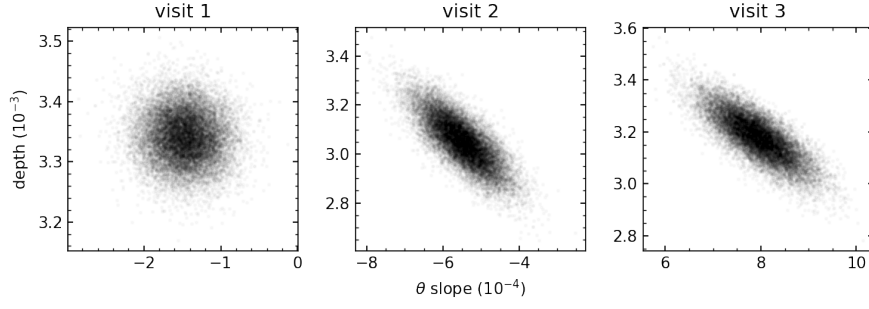


Fig. A.5. Correlation between the slope in time and transit depth of the systematic error model. This figure was produced by sampling the likelihood distribution of our model against its parameters using a Markov Chain Monte Carlo on the white-light curves. It shows that, apart from visit 1 where the transit mid-time is observed, the transit depth is correlated with the slope in time θ used to model systematics over the duration of a visit (a shallower slope is compensated by a deeper transit). As only the ingress and egress are observed in visits 2 and 3, we assume that the spectrum-to-spectrum differences in our study are partially due to this effect. However, as the visits-combined analysis contains a complete transit (in phase), the slope of the systematic error model should be less correlated with the transit depth, as in visit 1, which is confirmed by the similarity observed between visit 1 and the global spectrum (Figure 3)

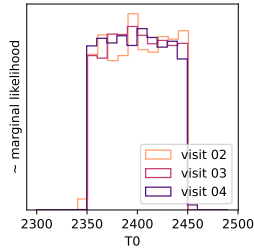


Fig. A.6. Corner plot of the parameters inferred in the 1T model. T_0 denotes the temperature of the cooler component)

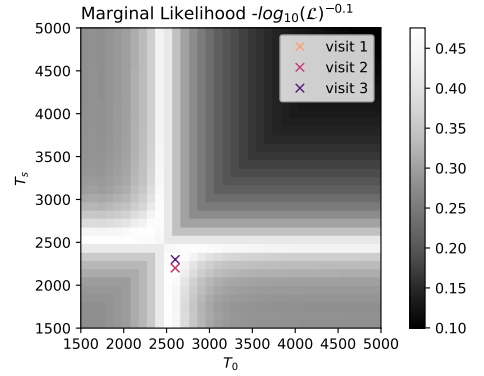


Fig. A.8. 2T model likelihood sampled on the temperature grids described in Table 4 and marginalized over the photospheric heterogeneity covering fractions. The symmetry of this distribution is simply due to the symmetry of our two-component model, with covering fractions f and $1 - f$.

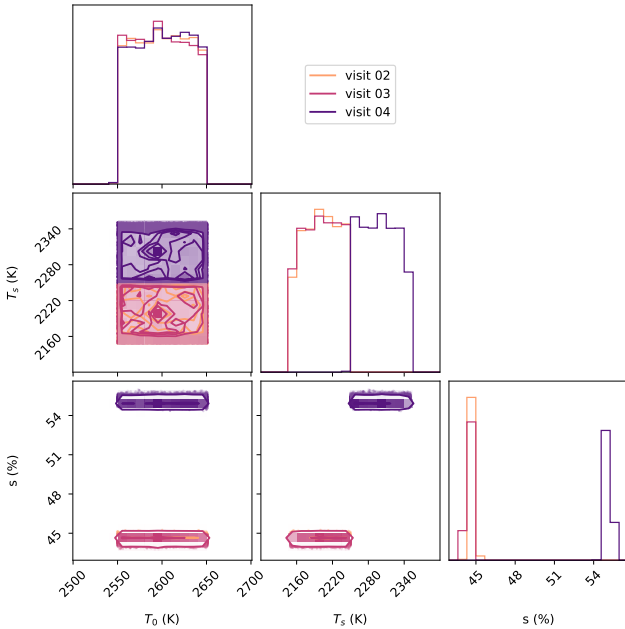


Fig. A.7. Corner plot of the parameters inferred in the 2T model. Here T_0 denotes the temperature of the quiescent component and T_s the temperature of the cooler component, with s its covering fraction. Visit 3 is better modeled with a cooler component at ~ 2300 K instead of ~ 2200 K for visit 1 and 2. We assume that this is likely due to the coarse grid of temperatures of our model, as the likelihood distribution seems to have a single maximum (see Figure A.8).

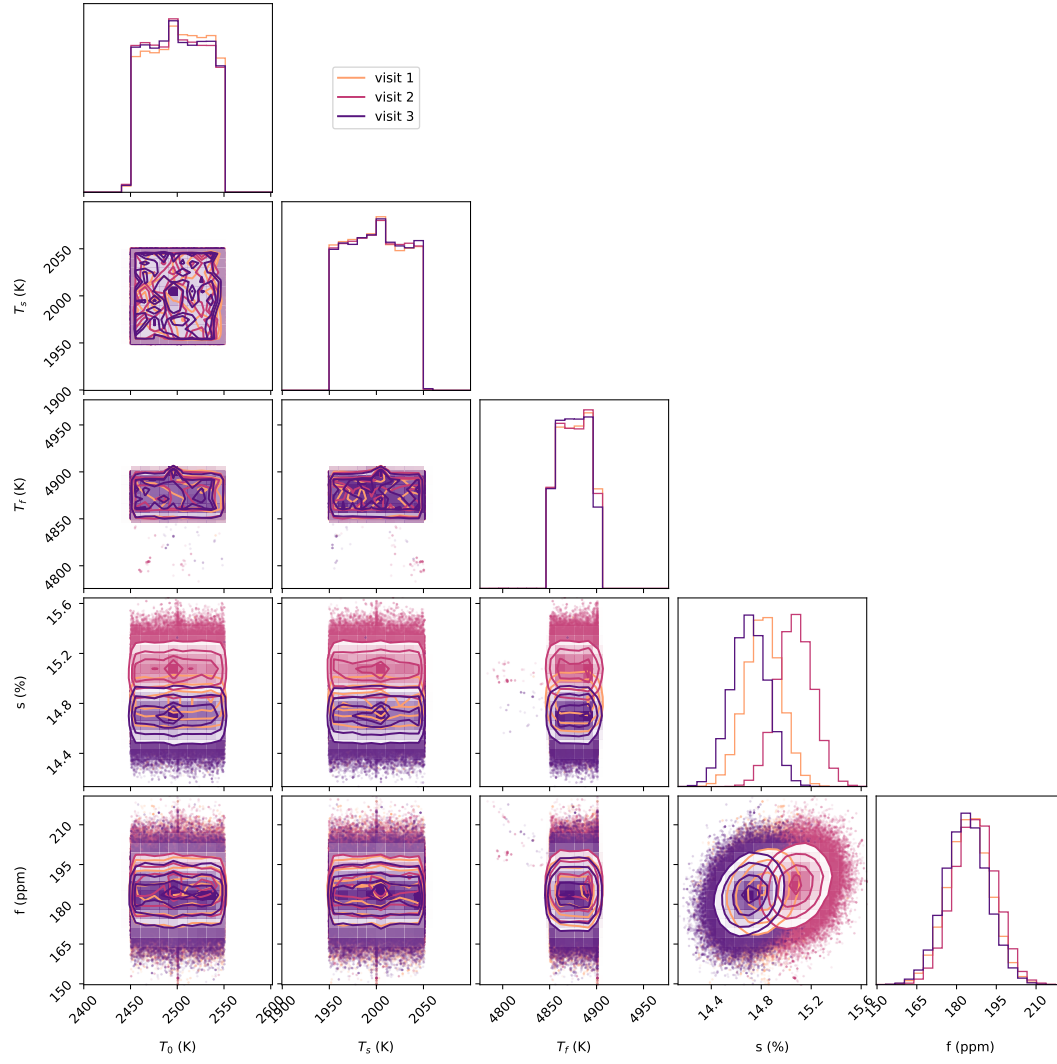


Fig. A.9. Corner plot of the parameters inferred in the 3T model. Here T_0 denotes the temperature of the quiescent component, T_s the temperature of the cooler component with s its covering fraction and T_f the temperature of the hotter component with f its covering fraction.

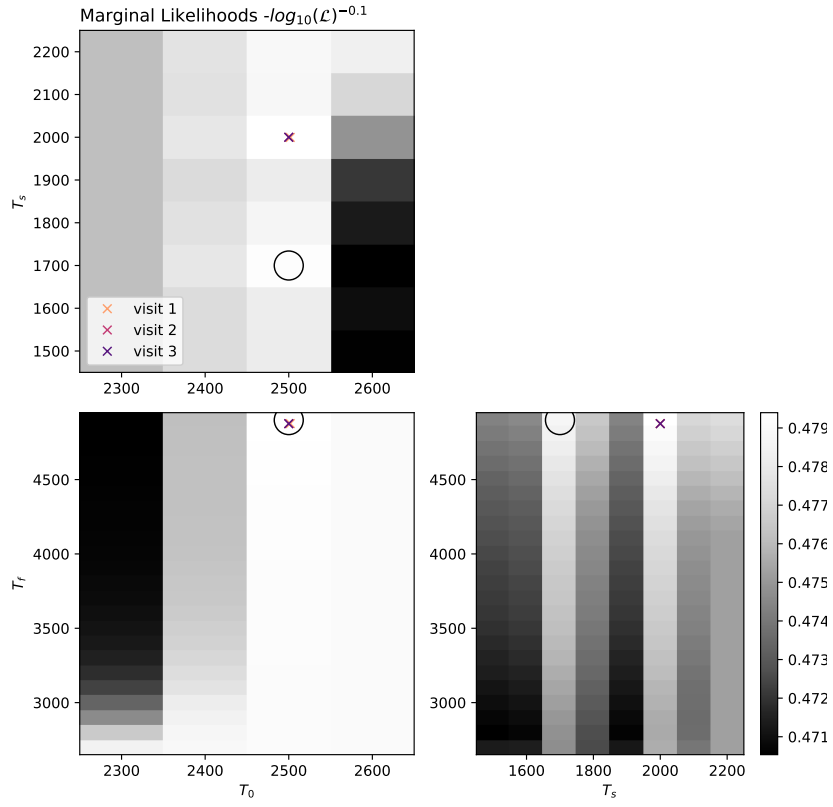


Fig. A.10. 3T model likelihood sampled on the temperature grids described in Table 4 and marginalized over the covering fractions of the photospheric heterogeneities, as well as the temperature of each component. For each visit, colored crosses correspond to the global maximum likelihood parameters. The black circle shows a local maximum of the likelihood distribution, highlighting the bimodal nature of the model.